

Relative grain boundary area and energy distributions in nickel

Jia Li, Shen J. Dillon¹, Gregory S. Rohrer*

Department of Materials Science and Engineering, Carnegie Mellon University, Pittsburgh, PA 15213, USA

Received 21 April 2009; received in revised form 7 May 2009; accepted 3 June 2009

Available online 1 July 2009

Abstract

The three-dimensional interfacial network of grain boundaries in polycrystalline nickel has been characterized using a combination of electron backscatter diffraction mapping and focused ion beam serial sectioning. These data have been used to determine the relative areas of different grain boundary types, categorized on the basis of lattice misorientation and grain boundary plane orientation. Using the geometries of the interfaces at triple lines, relative grain boundary energies have also been determined as a function of lattice misorientation and grain boundary plane orientation. Grain boundaries comprising (1 1 1) planes have, on average, lower energies than other boundaries. Asymmetric tilt grain boundaries with the $\Sigma 9$ misorientation also have relatively low energies. The grain boundary energies and areas are inversely correlated.

© 2009 Acta Materialia Inc. Published by Elsevier Ltd. All rights reserved.

Keywords: Nickel; Grain boundary energy; Microstructure; Electron backscattering diffraction (EBSD); Focused ion beam (FIB)

1. Introduction

It is well known that grain boundary energies are anisotropic and that the relative energies are influential in determining the polycrystalline structure and, as a result, the properties of the material [1]. In general, the grain boundary energy can vary as a function of all five macroscopic crystallographic parameters (three for lattice misorientation and two for grain boundary plane orientation) that are used to classify a grain boundary. Because of the large number of different grain boundaries, past measurements of grain boundary energies in face-centered cubic (fcc) metals have been made over a limited range of the crystallographic parameters [2–16]. In this paper, we report the relative grain boundary energies of nickel as a function of all macroscopic five crystallographic parameters, a quantity that will be referred to as the grain boundary energy distribution (GBED). Nickel is used in a wide range of structural appli-

cations where both strength and corrosion resistance are required, and its properties have been correlated with the structure of the grain boundary network [17–20].

The first comprehensive measurement of the grain boundary energy distribution was carried out for MgO, a ceramic with the rock salt structure [21]. The study showed that the grain boundary energy varied with both the lattice misorientation and the grain boundary plane orientation. The energy variation over the grain boundary orientation parameters was closely related to the variation in the free surface energy. Furthermore, the grain boundary character distribution (GBCD) was inversely correlated to the GBED. If the latter observation reflects a general phenomenon that occurs in a steady-state microstructure, then it suggests that it should be possible to control the GBCD by changing the GBED through the addition of impurities that segregate to grain boundaries [22]. The objective of this work was to determine the relationship between the GBCD and GBED in Ni and to test the generality of the previous observations.

The GBED and GBCD measurements in MgO were accomplished using extensive electron backscatter diffraction (EBSD) mapping coupled with manual serial section-

* Corresponding author. Tel.: +1 412 268 2696; fax: +1 412 268 3113.

E-mail address: gr20@andrew.cmu.edu (G.S. Rohrer).

¹ Present address: Department of Materials Science and Engineering, University of Illinois, Urbana-Champaign, IL, USA.

ing [21,23]. Because the procedures are experimentally challenging, only a single similar measurement has been carried out since this time and this example included only a limited number of boundaries [24]. In the intervening years, however, there have been two significant innovations. First, the speed of EBSD mapping has improved by more than a factor of 10. Secondly, the development of the dual beam focused ion beam (DB-FIB) scanning electron microscope makes it possible to record an orientation map on a surface and then remove a thin section by ion milling and record another orientation map on a parallel layer, thereby automating the time-consuming serial sectioning process. The possibility of recording parallel EBSD maps and reconstructing the grain shapes in three dimensions has already been demonstrated [25–28]. Here, we used these techniques to determine the geometries of grain boundaries meeting at triple junctions and use this information to determine the GBCD and GBED.

2. Methods

2.1. Experimental methods

A 5 mm polycrystalline Ni rod (99.999% Ni, Alfa Aesar-Puratronic) was sectioned to produce specimens. The sections were cross-rolled to 70% deformation, then ground using SiC abrasive paper. The cold-worked samples were then annealed in a flowing hydrogen atmosphere at 300–350 °C for 30 min. This treatment fully recrystallized the material, which was then electropolished in an electrolyte composed of 70%/30% nitric acid/methanol at a temperature of –50 °C for 20 s. This procedure produced a smooth crystalline surface suitable for EBSD.

The orientation mapping and serial sectioning was carried using a DB-FIB (Nova 600, FEI Company, Hillsboro, OR). With the sample mounted on a 45° pre-tilted stub, it may be tilted 7° toward the ion-beam in the FIB or rotated 180° and tilted 25° towards the EBSD detector for data collection (EDAX, Mahwah, NJ). An area on the very edge of the sample was selected for examination. It is important that the sample be well aligned so that the amount of material milled away in each step is consistent and controlled. Alignment is also important to ensure that the EBSD maps are being collected from the same region in subsequent steps. Circular fiducial markers were therefore milled into the lateral surfaces of the samples and, during the automated data collection, were used to align the area of interest during subsequent milling and EBSD mapping steps [25,26]. Automation of the procedure was performed using control scripts in the FEI runscript language. The sample was ion-milled at 30 kV and 5 nA using a Ga⁺ ion beam. EBSD data were acquired using a 30 kV beam at a current of 9.5 nA. The slice thickness between subsequent serial sections was 200 nm and the in-plane resolution of the EBSD scans was 200 nm. The EBSD patterns were binned to 8 × 8 and collected at approximately 100 points per second so that about 30 min were needed to record each map.

The data presented here are the combination of data from five separate regions. Each region was approximately 80 × 100 × 6 μm. In the total volume, there were approximately 1250 grains, with an average grain diameter of 11 μm. One of the five sections, comprising 30 parallel layers, is illustrated in Fig. 1.

2.2. Data processing

The EBSD data were processed exactly as described in a recent paper [29]. Briefly, an average orientation was determined for each grain larger than 10 pixels. The grain boundaries were then approximated by a set of line segments. Triple points (where three grain boundary line segments intersect) on adjacent layers were compared and if they were found to have similar locations and similar adjoining crystal orientations, a triple line was constructed to connect the two points. This process was used to identify about 37,000 triple lines. Knowing the triple line direction and the grain boundary line segments that connect on the layers above and below, grain boundary plane orientations can be determined from the cross products of each grain boundary line segment and the triple line connecting the layers. Each cross product yields a grain boundary normal vector and an area so that the 37,000 triple lines yielded 222,000 normal vectors. These quantities are classified in a discrete matrix of grain boundary types.

The data were acquired with equal spacing of the orientation points in the plane of the sample and between planes. This leads to a coarse discretization of the grain boundary plane orientations in the laboratory reference frame. To reduce the negative effects of the discretization, the triple lines were connected between alternating layers so that the vertical discretization is coarser than the horizontal discretization. The alignment of the data is also very important. The TSL software can be used to align the data to the nearest pixel on the fixed grid. However, when one examines the orientations of the triple lines, they are typically biased [29]. Assuming that the triple lines should be randomly oriented, their average position should be normal to the milling direction. To correct for the effect, a rigid offset is applied to each layer so that the mean of

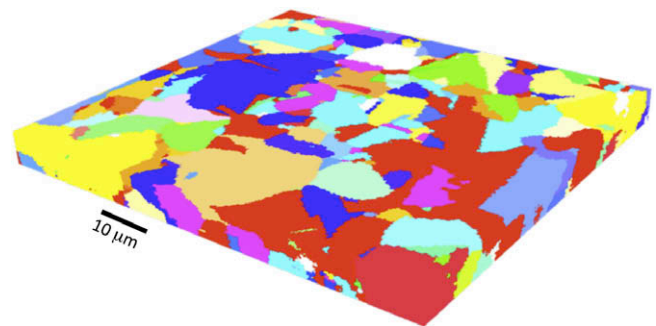


Fig. 1. Three-dimensional reconstruction of polycrystalline Ni. This section of the data contains 30 layers and the volume is 85 μm × 75 μm × 6 μm. The grains are colored by orientation.

the triple line direction is normal to the sample surface. In most cases, these adjustments are less than the pixel spacing.

2.3. Grain boundary energy reconstruction

The calculation of the grain boundary energies was carried out using the capillarity vector method developed by Morawiec [30]. The method was described in detail and tested by simulation in Ref. [30]. Later, the same method was used to determine the grain boundary energies of MgO [21]. The energy calculations presented here were carried out in exactly the same way, using the same computer programs that were used in Refs. [21,30].

The capillarity vector reconstruction method is similar to many other interface energy measurements in that the experimental observable is the interfacial geometry; the energy is computed from the geometry using an expression for interfacial equilibrium. In this case, the equilibrium at the triple line is described by the Herring [31] equation. Therefore, the key assumption underpinning this and previous measurements of relative grain boundary energies is that the interfacial junctions are in local thermodynamic equilibrium. In the capillarity vector reconstruction method, the Herring [31] condition is expressed in terms of capillarity vectors, as formulated by Hoffman and Cahn [32,33]:

$$(\zeta^1 + \zeta^2 + \zeta^3) \times \mathbf{l} = 0 \quad (1)$$

where ζ^1 , ζ^2 and ζ^3 are the capillarity vectors associated with the three grain boundaries and \mathbf{l} is the triple line. Each capillarity vector has a component perpendicular to the grain boundary whose magnitude is equal to the relative grain boundary energy. Each capillarity vector also has a component tangent to the boundary whose magnitude is the differential of the energy with respect to a right-handed rotation about \mathbf{l} .

As mentioned above, we have characterized the normal and tangent vectors for 37,000 grain boundary triple junctions and can apply Eq. (1) to each junction. The unknowns are the magnitudes of the capillarity vectors. The data are discretized as described earlier, so there is one ζ vector for each discrete boundary type. An iterative procedure is then used to find the set of ζ that most nearly satisfy the 37,000 equilibrium equations. In this calculation, we use a relaxation factor, which controls the magnitude of changes applied to each capillarity vector during subsequent iterations, of 0.02. After 300 iterations, the change in the sum of the magnitude of all of the changes is less than 1% of the change during the first iteration. The final result was smoothed by replacing the value of ζ in each cell with the average of that vector and the vectors in the adjacent cells. Finally, the energy (γ) of each discrete grain boundary type is given by $\gamma = \zeta \cdot \mathbf{n}$, where \mathbf{n} is the grain boundary normal. Previous calculations using simulated data based on model energy functions showed that the capillarity vector method reproduced all of the trends in the

function, but did not quantitatively reproduce the depths of cusps [21,30]. Based on these findings, it is assumed that the actual GBED is more anisotropic than the reconstructed distribution presented here.

3. Results

The discretization of the GBCD and GBED was carried out exactly as described in Ref. [34]. As the discretization becomes finer, the resolution increases, but there are also many more grain boundary types and, therefore, more observations are needed to accurately sample the distribution. In the present case, we performed the analysis at two different levels of discretization: nine bins per 90° (10° resolution) and 11 bins per 90° (8.2° resolution). For the case of 10°, 97% of all bins contained at least 10 observations. For the case of 8.2° resolution, 85% of the bins contained five or more observations. The distributions computed at the two resolutions were qualitatively the same, so the GBCD and GBED determined with 8.2° resolution are presented here.

We begin by considering the distribution of grain boundary planes in the crystal reference frame (see Fig. 2a). This distribution does not consider the grain boundary misorientation. The minimum of the distribution occurs at (1 0 0) and the maximum occurs at (1 1 1). This is consistent with other fcc metals, including aluminum [35], brass [36] and copper [37]. The (1 1 1) plane is the closest packed and the habit plane for the twin, so it is presumed to have the lowest energy. This is confirmed by the result in Fig. 2b, which shows the relative energy of the grain boundary planes, in the crystal reference frame. The minimum energy occurs at the (1 1 1) orientation and the maximum at the (1 0 0) position. In other words, when the lattice misorientation is ignored, the grain boundary energy is inversely correlated to the population.

The GBCD and GBED for the $\Sigma 3$ grain boundary are compared in Fig. 3. Fig. 3a shows the distribution of grain boundary planes in the bicrystal reference frame for all grain boundaries with a 60° misorientation about [1 1 1] plotted on a stereographic projection. The GBCD is strongly peaked at the position of the coherent twin, which is the pure twist boundary bounded on both sides by (1 1 1) planes. In this case, the logarithm of the population is plotted so that the tails of the peak are visible. The relative energies of $\Sigma 3$ boundaries with different grain boundary plane orientations are plotted in Fig. 3b. The minimum of the energy occurs at the position of the coherent twin where the population is maximized. The energy of the twin is the global minimum of the entire GBED (all misorientations) and the relative area of the twin is the global maximum of the GBCD.

The GBCDs and GBEDs for the $\Sigma 5$ and $\Sigma 7$ misorientations are compared in Fig. 4. These particular misorientations are selected as examples of boundaries that do not make up a significant fraction of the population and should not be considered to have any special characteristics. Both

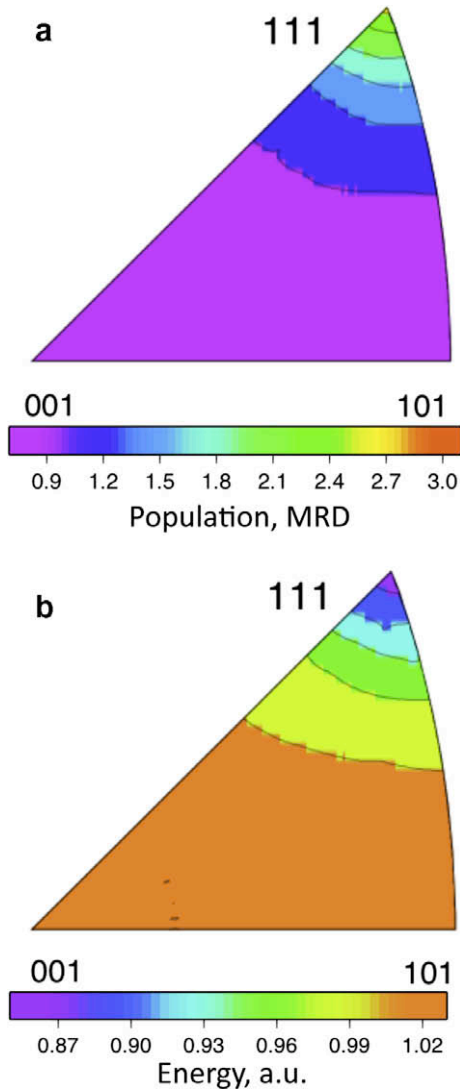


Fig. 2. (a) Distribution of grain boundary planes in the crystal reference frame, plotted in stereographic projection. (b) Relative grain boundary energies with respect to the crystal reference frame.

of these grain boundaries occur less frequently than would be expected in a random distribution. For the $\Sigma 5$ boundary, the pure twist positions (at $[1\ 0\ 0]$ and $[\bar{1}\ 0\ 0]$) and the pure tilt positions (along the $[1\ 0\ 0]$ zone) are least frequently populated. These are also the positions of maximum energy. For the $\Sigma 7$ grain boundary, the peak population and minimum energy coincide at the orientation of the $(1\ 1\ 1)$ twist grain boundary and, as with $\Sigma 5$, there is an approximate inverse correlation between the population and the energy.

The GBCD and GBED for the $\Sigma 9$ grain boundary are compared in Fig. 5. In agreement with prior stereological results [37], the population of $\Sigma 9$ grain boundaries peaks along the zone of pure tilt grain boundaries and the maxima occur at the orientations of the planes associated with $(\bar{1}\ 1\ 1)/(\bar{1}\ 1\ 5)$ asymmetric tilt boundaries. The energy distribution displays an approximate inverse correlation with the area distribution, with the minima occurring along the $[1\ 1\ 0]$ zone, which matches the orientations of the asymmetric tilt boundary. However, there are other features in Fig. 5 that are not so well correlated.

The relative energies of symmetric $[1\ 1\ 0]$ tilt grain boundaries have been measured for Al [4,5] and Cu [11]. The energies of these same boundaries have also been calculated for Cu and Au [38,39] and Al [40]. For comparison, the relative energies the symmetric $[1\ 1\ 0]$ tilt grain boundaries were extracted from the current data on Ni. The results are plotted as a function of tilt angle (see Fig. 6) and they show a minimum at the orientation of the coherent twin (70.5°). There are also clear cusps as the position of the two $\Sigma 9$ grain boundaries. The boundary at 39° is terminated by $(2\ 2\ 1)$, while the boundary at 141° is terminated by $(1\ \bar{1}\ 4)$. The data in the range of $95\text{--}125^\circ$ appear scattered and the minima are not thought to represent cusps.

To illustrate the average relationship between the grain boundary energy and population, the grain boundary energies were categorized into evenly spaced bins of width 0.1

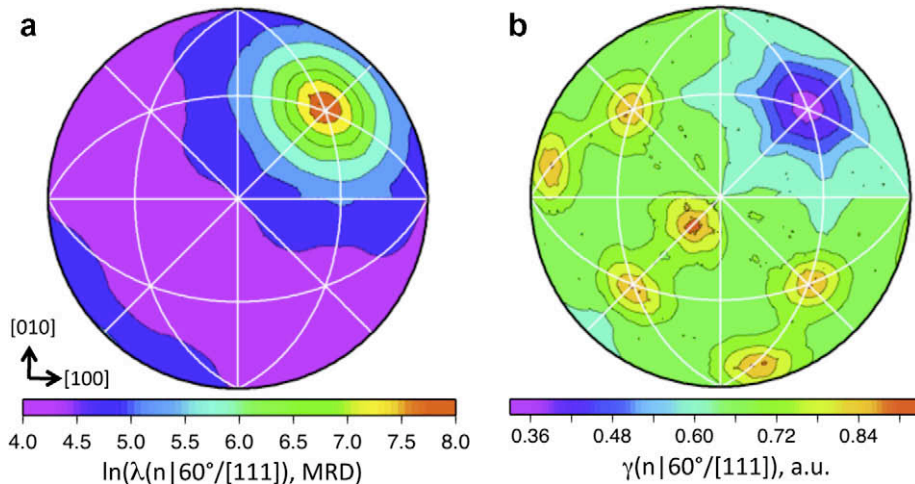


Fig. 3. (a) Grain boundary plane distribution compared to (b) the grain boundary energy distribution for grain boundaries with the $\Sigma 3$ misorientation. The plots are stereographic projections, in the bicrystal reference frame, and the $[0\ 0\ 1]$ axis is vertical and in the center of the plots. The logarithm of the population is plotted in (a).

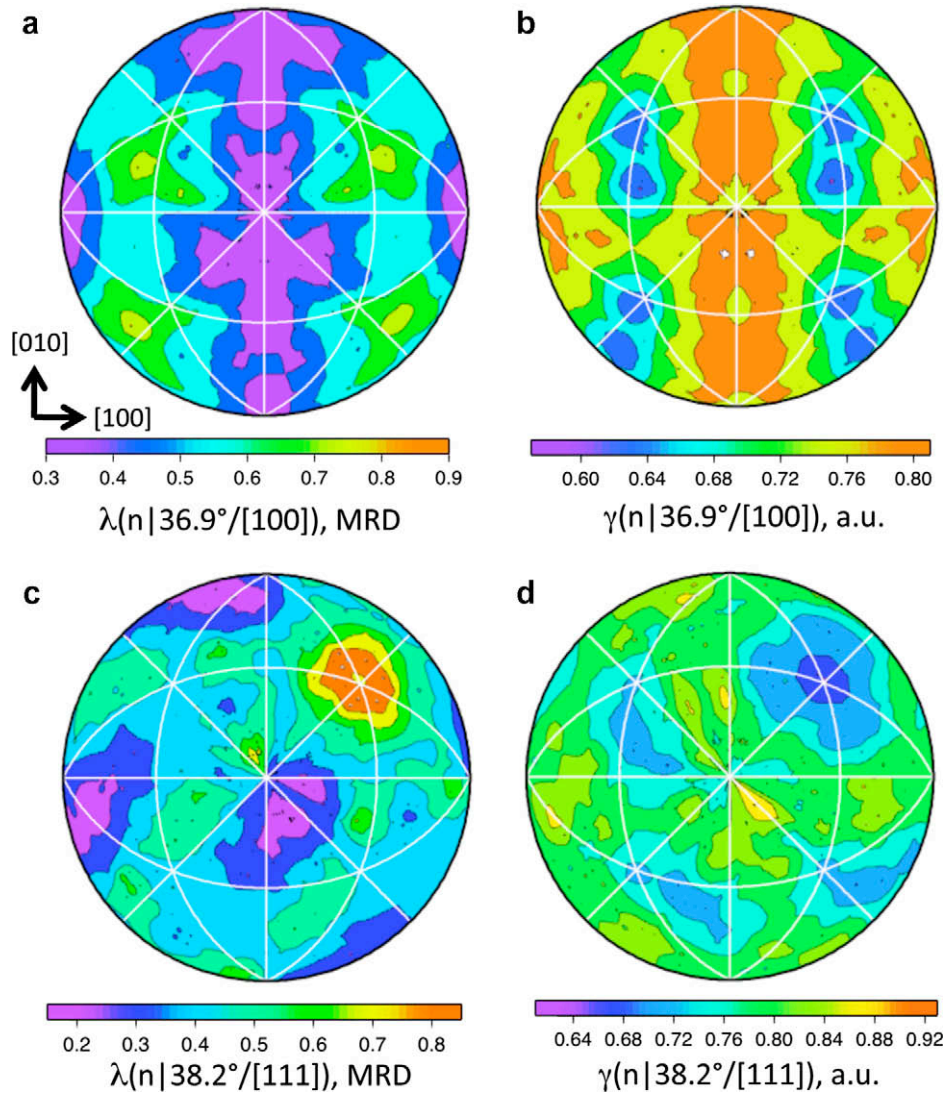


Fig. 4. (a and c) Grain boundary plane distributions compared to (b and d) the grain boundary energy distributions for grain boundaries with the $\Sigma 5$ (a and b) and $\Sigma 7$ (c and d) misorientations. The plots are stereographic projections, in the bicrystal reference frame, and the $[0\ 0\ 1]$ axis is vertical and in the center of the plots.

a.u. and the average population of all of the boundaries in each bin was then determined. The logarithms of these average values are shown in the plot in Fig. 7. These data show that, on average, the grain boundary population of a material is inversely correlated to the relative grain boundary energy.

4. Discussion

Using the data from planar sections, it is possible to get a reliable estimate of the total fractional area of coherent twins within the microstructure [41]. For all boundary segments with the $\Sigma 3$ misorientation (within Brandon's [42] criterion), the orientation of the segment can be compared to the orientation of the ideal twin plane. If the segment is within $\pm 10^\circ$ of the ideal orientation, it is assumed to be a coherent twin. Analyzing our data in this way, we find that twin boundaries make up 28.6% of all of the grain bound-

ary length observed on the plane sections. With the 8.2° discretization, there are approximately 17,894 discrete grain boundary types. So, assuming all of the twins are classified as a single type, the distribution at this point should have a value of 5100 MRD. The computed value is 4500 MRD and differs by only 12% from the ideal value, so we assume that the calculations used to analyze the data and create the distribution are sufficiently accurate.

Because the twins serve as an "internal standard" for this measurement, we were able to test the efficacy of several of our procedures. For example, both decreasing the in-plane to between-plane pixel spacing ratio and the subpixel alignment procedure improved the accuracy of the data, as judged by the value of the distribution at the position of the coherent twin. It should also be mentioned that using the twins as an internal standard is problematic with our discretization scheme when there are nine bins for every 90° . The ideal Euler angles for the twin misorienta-

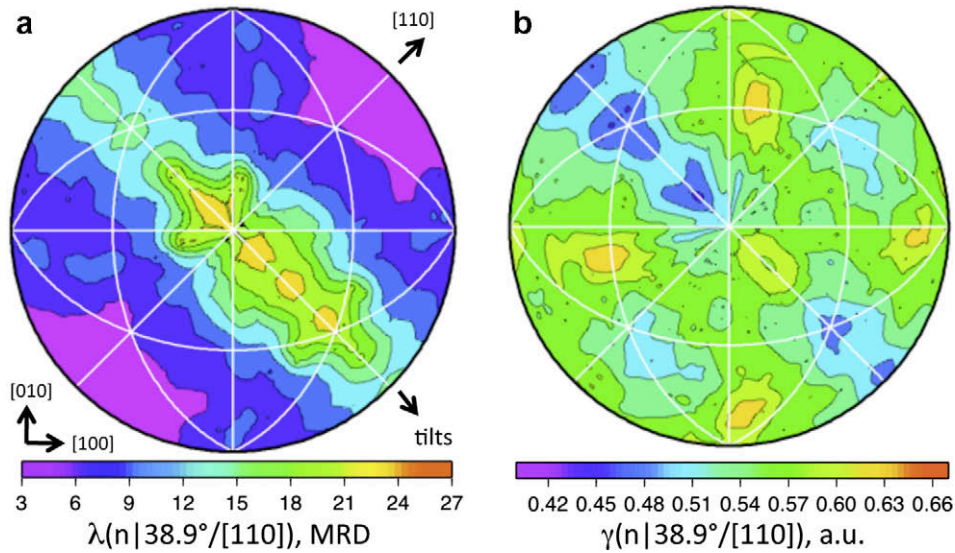


Fig. 5. (a) Grain boundary plane distribution compared to (b) the grain boundary energy distribution for grain boundaries with the $\Sigma 9$ misorientation. The plots are stereographic projections, in the bicrystal reference frame, and the $[001]$ axis is vertical and in the center of the plots.

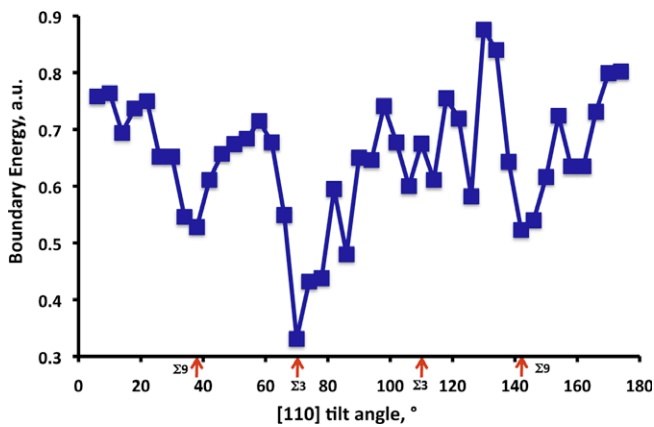


Fig. 6. The relative energies of $[001]$ symmetric tilt grain boundaries. Red arrows on the horizontal axis denote the positions of the grain boundaries with the $\Sigma 3$ and $\Sigma 9$ misorientations. (For interpretation of the references to colour in this figure legend, the reader is referred to the web version of this article.)

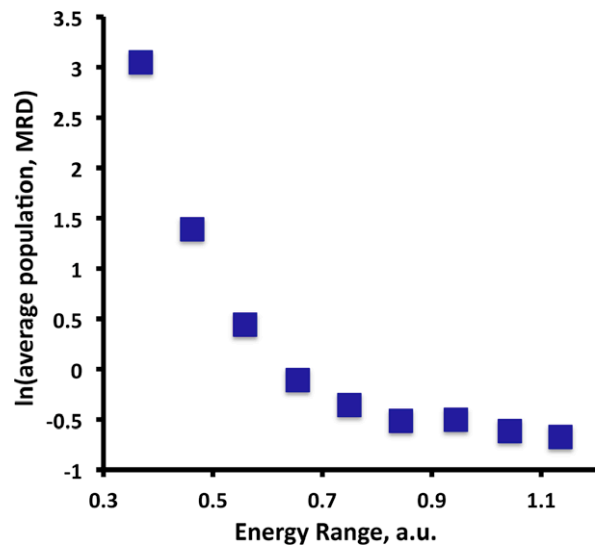


Fig. 7. The average populations of all grain boundaries with energies that are within the range of ± 0.05 a.u. of the energy on the horizontal axis.

tion are $\phi_1 = 45^\circ$, $\Phi = 70.5^\circ$, $\phi_2 = 45$. Because it is $\cos \Phi$ that is discretized, the limits of each bin occur at intervals of $1/9$. For the coherent twin, $\cos \Phi = 3/9$ and it therefore falls exactly on the border between bins. Unless the boundaries between bins are shifted, the population of the twin is split between multiple bins and always appears to have a lower than expected population when using 10° resolution.

The current method of evaluating the GBCD has a number of limitations. For example, the grain boundary character distribution is determined only from triangular segments near the triple junctions. The segments of grain boundaries that are not directly connected to a triple junction are not included in the distribution. However, despite this limitation, the distributions reported here are comparable to previously reported distributions for

Ni determined from the stereological analysis of two-dimensional sections [37]. A second limitation is that the networks of triple lines and triangular segments measured here does not form a continuous interfacial mesh, as would be needed for input into a finite element simulation.

Consistent with many previous studies of grain boundaries in Ni, the population of $\Sigma 9$ tilt boundaries is quite high; $\Sigma 9$ grain boundaries make up 8.84% of all the grain boundary length and most of them are tilt grain boundary boundaries. It is well known that if two $\Sigma 3$ grain boundaries meet, and they do not share a common axis of rotation, they must join a $\Sigma 9$. In this sample, 38.6% of the total grain boundary length is composed of $\Sigma 3$ grain

boundaries, so it stands to reason that some pairs of the $\Sigma 3$ boundaries will meet at a $\Sigma 9$ boundary. In fact, nearly one-quarter of all the junctions are made up of two $\Sigma 3$ boundaries and one $\Sigma 9$ boundary. Furthermore, in the case where the two $\Sigma 3$ boundaries are coherent twins, the grain boundary plane of the $\Sigma 9$ boundary is confined to the $\langle 110 \rangle$ zone, which makes it a tilt boundary. This leads to the question, do $\Sigma 9$ tilt grain boundaries occur with a high frequency because they have low energies or are they a crystallographic artifact of the intersections of $\Sigma 3$ boundaries? According to the results here, they do have low energies, and this is consistent with their high population. However, note that along the $[1\ 1\ 0]$ zone the exact positions of the maxima and minima are exactly correlated for only the $(\bar{1}11)/(1\bar{1}5)$ asymmetric boundary. For configurations with low populations, some scatter is expected because of the limited number of observations. However, this does not apply to the $\Sigma 9$ tilt boundaries, which have relatively large populations. The origin of the mismatch between some of the peaks and valleys is not presently understood.

For $[1\ 1\ 0]$ symmetric tilt grain boundaries in Al, Hasson et al. [4,5] found energy minima at the coherent twin position and at the symmetric $(1\bar{1}3)$ $\Sigma 11$ grain boundary. Grain boundary energies determined by atomistic calculations agree with this observation [38–40]. According to the current observations of Ni, the minima are found at the twin and at both of the symmetric $\Sigma 9$ grain boundaries. While the $(1\bar{1}4)$ $\Sigma 9$ boundary and the $(1\bar{1}3)$ $\Sigma 11$ boundary are separated by only 11° and there is undoubtedly some overlap, the average energy at $\Sigma 9$ is (0.57) distinctly lower than the average value at $\Sigma 11$ (0.76). Prior measurements of $[1\ 1\ 0]$ symmetric tilt grain boundaries in Cu at different temperatures suggest that, as the temperature is decreased, the minimum shifts from the $(1\bar{1}3)$ $\Sigma 11$ position to the $(1\bar{1}4)$ $\Sigma 9$ position [11]. To minimize grain growth, the microstructures on which the present measurements were conducted were annealed at relatively low temperatures, so the present data should be more comparable to the low temperature data from Ref. [11], which showed the minimum at $(1\bar{1}4)$. Unfortunately, there are no similar measurements of Ni that can be used for comparison. It should also be noted that the minima on Fig. 7 at the positions of the symmetric $\Sigma 9$ tilt boundaries occur not because they are symmetric, but because all $\Sigma 9$ boundaries have relatively low energies. As mentioned before, the lowest energy $\Sigma 9$ grain boundaries are asymmetric $(\bar{1}11)/(1\bar{1}5)$ pairs.

Although the materials and temperature differ, it is also interesting to compare the present observations to a previous combined experimental and theoretical study of $\Sigma 3$ grain boundaries in Cu, with boundary plane orientations in the $\langle 110 \rangle$ zone [10]. The common feature between Cu and Ni is that they share the fcc crystal. The previous work shows that the grain boundary energy increases with the angle of inclination away from the perfect coherent twin. After reaching a maximum at about 70° of inclination,

there is a weak local minimum just before the $\{2\ 1\ 1\}/\{2\ 1\ 1\}$ symmetric tilt grain boundary [10]. This is similar to what is shown in Fig. 3b.

The trend in the data that the grain boundary energy distribution is inversely related to the grain boundary plane distribution is similar to that found previously for MgO [21]. A model has recently been proposed to explain the existence of a steady-state grain boundary character distribution that is inversely related to the grain boundary energy distribution [43,44]. The model is based on the experimental observation that during grain growth higher energy boundaries are more likely to be decreasing in area and lower energy boundaries are more likely to be increasing in area [44]. Based on this, if one assumes that the rate at which grain boundaries are eliminated from the system during critical events is proportional to the grain boundary energy, then steady-state distributions with an inverse correlation are produced [43].

It should be noted that the observed inverse correlation between population and energy is consistent with numerous simulations of grain growth in which anisotropic grain boundary energies have been assumed [45–49]. Interestingly, the same simulations show that grain boundary mobility has a very weak influence on the grain boundary character distribution. However, it should be noted that these conclusions apply only to cases in which the polycrystal is relatively untextured, evolves by normal grain growth, has reached a scale invariant structure and does not have intergranular films or other second phases that affect grain boundary motion. When this is not the case, there are mechanisms that can sustain high mobility grain boundaries, even after they grow past an immediate neighbor and are annihilated. For example, if a grain is growing into a textured matrix with similarly oriented grains, then every time the high mobility boundary is annihilated, a new boundary with similar character and mobility is formed [50]. Furthermore, if the characteristic of a grain boundary that gives it high mobility is its composition, this can also be sustained as the crystallographic characteristics changes. For example, boundaries that undergo complexion transitions can sustain their high mobilities even as their crystallography changes [51,52]. In fact, a recent study of alumina evolving by abnormal growth shows that consistent grain boundary character distributions are not obtained [53].

Based on the data presented here, the characteristic associated with low energy grain boundaries in Ni is the $(1\ 1\ 1)$ grain boundary plane orientation, as illustrated in Fig. 2. This characteristic appears to be more important than the value of Σ . For example, the $\Sigma 5$ and $\Sigma 7$ boundaries have the second and third highest lattice coincidences, but they are neither low in energy nor high in population. The $\Sigma 9$, on the other hand, which has relatively lower coincidence than $\Sigma 5$ and $\Sigma 7$, has a low average energy. The $\Sigma 3$ boundary is a special case, where the twin consists of two $(1\ 1\ 1)$ surfaces with essentially no in-plane distortion of the atomic positions.

5. Conclusions

The grain boundary energy distribution of Ni varies with both lattice misorientation and grain boundary plane orientation. In general, grain boundaries terminated by (1 1 1) planes have lower energies than others. In addition to the twins, $\Sigma 9$ tilt boundaries have relatively low energies, and asymmetric tilt boundaries are the lowest of these energies. The results support the idea that for scale-invariant microstructures evolving by normal grain growth, on average, the relative areas of different types of grain boundaries in polycrystals are inversely correlated to the relative grain boundary energies.

Acknowledgements

This work was primarily supported by the MRSEC program of the National Science Foundation under Award Number DMR-0520425. Partial support by the Pennsylvania DCED is also acknowledged.

References

- [1] Smith CS. *Trans AIME* 1948;175:15.
- [2] Read WT, Shockley W. *Phys Rev* 1950;78:275.
- [3] Gjostein NA, Rhines FN. *Acta Met* 1959;7:319.
- [4] Hasson GC, Goux C. *Scripta Met* 1971;5:889.
- [5] Hasson G, Boos J-Y, Herbeuval I, Biscondi M, Goux C. *Surf Sci* 1972;31:115.
- [6] McLean M. *J Mater Sci* 1973;8:571.
- [7] Chan S-W, Balluffi RW. *Acta Met* 1985;33:1113.
- [8] Chan S-W, Balluffi RW. *Acta Met* 1985;34:2191.
- [9] Schmelzle R, Muschlik T, Gust W, Predel B. *Scripta Met Mater* 1991;25:1981.
- [10] Wolf U, Ernst F, Muschik T, Finnis MW, Fischmeister HF. *Philos Mag A* 1992;66:991.
- [11] Miura H, Kato M, Mori T. *J Mater Sci Lett* 1994;13:46.
- [12] Straumal BB, Polyakov SA, Bischoff E, Gust W, Mittemeijer EJ. *Interface Sci* 2001;9:287.
- [13] Skidmore T, Buchheit RG, Juhas MC. *Scripta Mater* 2004;50:873.
- [14] Amouyal Y, Rabkin E, Mishin Y. *Acta Mater* 2005;53:3795.
- [15] Barmak K, Kim J, Kim C-S, Archibald WE, Rohrer GS, Rollett AD, et al. *Scripta Mater*. 2006;54:1059.
- [16] Amouyal Y, Rabkin E. *Acta Mater* 2007;55:6681.
- [17] Palumbo G, Aust KT. *Acta Met* 1990;38:2343.
- [18] Lin P, Palumbo G, Erb U, Aust KT. *Scripta Met* 1995;33:1387.
- [19] Crawford DC, Was GS. *Met Trans A* 1992;23:1195.
- [20] Kumar M, King WE, Schwartz AJ. *Acta Mater* 2000;48:2081.
- [21] Saylor DM, Morawiec A, Rohrer GS. *Acta Mater* 2003;51:3675.
- [22] Pang Y, Wynblatt P. *J Am Ceram Soc* 2005;88:2286.
- [23] Saylor DM, Morawiec A, Rohrer GS. *Acta Mater* 2003;51:3663.
- [24] Rowenhorst DJ, Voorhees PW. *Met Mater Trans A* 2005;36:2127.
- [25] Uchic MD, Groeber MA, Dimiduka DM, Simmons JP. *Scripta Mater* 2006;55:23.
- [26] Groeber MA, Haley BK, Uchic MD, Dimiduk DM, Ghosh S. *Mater Charact* 2006;57:259.
- [27] Konrad J, Zaefferer S, Raabe D. *Acta Mater* 2006;54:1369.
- [28] Lewis AC, Jordan KA, Geltmacher AB. *Met Mater Trans A* 2008;39:1109.
- [29] Dillon SJ, Rohrer GS. *J Am Cer Soc*, in press. doi:10.1111/j.1551-2916.2009.03064.x.
- [30] Morawiec A. *Acta Mater* 2000;48:3525.
- [31] Herring C. Surface tension as a motivation for sintering. In: Kingston WE, editor. *The physics of powder metallurgy*. New York: McGraw-Hill; 1951. p. 143–79.
- [32] Hoffman DW, Cahn JW. *Surf Sci* 1972;31:368.
- [33] Cahn JW, Hoffman DW. *Acta Met* 1974;22:1205.
- [34] Rohrer GS, Saylor DM, El-Dasher BS, Adams BL, Rollett AD, Wynblatt P. *Z Met* 2004;95:197.
- [35] Saylor DM, El-Dasher BS, Rollett AD, Rohrer GS. *Acta Mater* 2004;52:3649.
- [36] Rohrer GS, Randle V, Kim C-S, Hu Y. *Acta Mater* 2006;54:4389.
- [37] Randle V, Rohrer GS, Miller HM, Coleman M, Owen GT. *Acta Mater* 2008;56:2363.
- [38] Wolf D. *Acta Metall Mater* 1990;38:781.
- [39] Wolf D. *J Mater Res* 1990;5:1708.
- [40] Tschopp MA, McDowell DL. *Philos Mag* 2007;87:3871.
- [41] Wright SI, Larsen RJ. *J Microsc* 2002;205:245.
- [42] Brandon DG. *Acta Met* 1966;14:1479.
- [43] Rohrer GS, Gruber J, Rollett AD. *Ceram Trans* 2009;201:343.
- [44] Dillon SJ, Rohrer GS. *Acta Mater* 2009;57:1.
- [45] Holm EA, Hassold GN, Miodownik MA. *Acta Mater* 2001;49:2981.
- [46] Upmanyu M, Hassold GN, Kazaryan A, Holm EA, Wang Y, Patton B, et al. *Interface Sci* 2002;10:201.
- [47] Kazaryan A, Wang Y, Dregia SA, Patton BR. *Acta Mater* 2002;50:2491.
- [48] Kinderlehrer D, Livshits I, Rohrer GS, Ta'asan S, Yu P. *Mater Sci Forum* 2004;467–470:1063.
- [49] Gruber J, George DC, Kuprat AP, Rohrer GS, Rollett AD. *Scripta Mater* 2005;53:351.
- [50] Rollett AD. *Mater Sci Forum* 2002;408–412:251.
- [51] Dillon SJ, Harmer MP. *Acta Mater* 2007;55:5247.
- [52] Dillon SJ, Tang M, Carter WC, Harmer MP. *Acta Mater* 2007;55:6208.
- [53] Dillon SJ, Miller HM, Harmer MP, Rohrer GS, submitted for publication.